PNAS RESEARCH ARTICLE | CHEMISTRY

In situ spectroelectrochemical probing of CO redox landscape on copper single-crystal surfaces

Feng Shao[a,b,c,1], Jun Kit Wong[c], Qi Hang Low[c,d], Marcella Iannuzzi[e], Jingguo Li[e,1,2], and Jinggang Lan[e,1,3]

Edited by Alexis Bell, University of California, Berkeley, CA; received October 4, 2021; accepted May 18, 2022

Electrochemical reduction of $CO_{(2)}$ to value-added chemicals and fuels is a promising strategy to sustain pressing renewable energy demands and to address climate change issues. Direct observation of reaction intermediates during the $CO_{(2)}$ reduction reaction will contribute to mechanistic understandings and thus promote the design of catalysts with the desired activity, selectivity, and stability. Herein, we combined in situ electrochemical shell-isolated nanoparticle-enhanced Raman spectroscopy and ab initio molecular dynamics calculations to investigate the CORR process on Cu single-crystal surfaces in various electrolytes. Competing redox pathways and coexistent intermediates of CO adsorption ($*CO_{atop}$ and $*CO_{bridge}$), dimerization (protonated dimer *HOCCOH and its dehydrated *CCO), oxidation ($*CO_2^-$ and $*CO_3^{2-}$), and hydrogenation (*CHO), as well as Cu-O_{ad}/Cu-OH_{ad} species at Cu-electrolyte interfaces, were simultaneously identified using in situ spectroscopy and further confirmed with isotope-labeling experiments. With AIMD simulations, we report accurate vibrational frequency assignments of these intermediates based on the calculated vibrational density of states and reveal the corresponding species in the electrochemical CO redox landscape on Cu surfaces. Our findings provide direct insights into key intermediates during the $CO_{(2)}$RR and offer a full-spectroscopic tool (40–4,000 cm^{-1}) for future mechanistic studies.

$CO_{(2)}$ reduction | in situ Raman | intermediates | AIMD | electrocatalysis

Significance

The electrochemical $CO_{(2)}$ redox reaction is a promising strategy to reduce carbon emissions by directly converting $CO_{(2)}$ into value-added fuels and chemicals. Understanding the reaction intermediates is of great significance for developing functional catalysts for $CO_{(2)}$ conversion. In this work, we combined in situ electrochemical shell-isolated nanoparticle-enhanced Raman spectroscopy with ab initio molecular dynamics calculations to investigate $CO_{(2)}$ redox reactions on Cu single-crystal surfaces under various conditions. We expect this understanding will provide new insights into the mechanisms of surface species for CO redox on Cu surfaces in alkaline solutions, which may facilitate the future design of new catalysts.

To convert intermittent and renewable energy (e.g., wind, solar, hydropower) into chemical fuels, the electrocatalytic $CO_{(2)}$ reduction reaction ($CO_{(2)}$RR) has become an attractive strategy, as it allows for high-density energy storage and greenhouse gas emission reduction (1–3). Among various electrocatalysts for $CO_{(2)}$RR, copper (Cu)-based materials are the most promising candidates to directly reduce $CO_{(2)}$ into valuable oxygenates and hydrocarbons, and one can tune their shapes, facets, pore sizes, interparticle distance, subsurface atoms, and grain boundaries to achieve specific activities and selectivities (1). Investigating reaction intermediates on Cu surfaces under working conditions will help us to understand the reaction mechanisms and to rationally design efficient catalysts. Yet, giving a complete spectroscopic characterization of all possible intermediates remains challenging, as competitive reactions coexist on Cu surfaces at low overpotentials. Possible reactions are i) the concerted/sequential proton-electron transfer for C_1 products (C_1 pathways) (4), ii) the decoupled proton-electron transfer for C–C couplings (C_2 pathways) (5), iii) the hydrogen evolution reaction (HER) (6), iv) the CO oxidation reaction (COOR) (7), and v) the water-gas shift reaction (8, 9). Therefore, a full-spectrum and molecular-level understanding of the heterogeneous $CO_{(2)}$RR under realistic electrochemical conditions is highly desirable. To this end, advanced in situ analytic methods combined with accurate theoretical simulations promise to identify various active intermediates and resolve competing pathways at Cu surfaces during the $CO_{(2)}$RR process (10, 11).

In situ spectroscopic approaches such as surface-enhanced Raman spectroscopy (SERS) (12–14), shell-isolated nanoparticle-enhanced Raman spectroscopy (SHINERS) (15), (surface-enhanced) infrared absorption spectroscopy (SEIRAS) (16–18), (attenuated total reflection) Fourier-transform infrared (FTIR) spectroscopy (19, 20), attenuated total reflection–surface-enhanced infrared absorption spectroscopy (ATR-SEIRAS) (21), and X-ray absorption/photoelectron spectroscopy (22, 23) have been widely employed to simultaneously identify key intermediates under working conditions and correlate them with theoretical mechanisms (2, 24). Several intermediates of the $CO_{(2)}$RR on Cu surfaces were previously proposed based on in situ/operando spectroscopic measurements (2). For example, a carboxylate anion $*CO_2^-$ was recognized by SERS as the first intermediate during the CO_2RR to form formate (C_1 pathways) (12), and SHINERS indicated the presence of surface $CuO_x/(OH)_y$ species under CORR conditions (15). In addition, surface-adsorbed *CO species that were in dynamic equilibrium with dissolved CO and could be asymmetrically displaced by surface *H species

Author contributions: F.S., J. Li, and J. Lan designed research; F.S., J.K.W., Q.H.L., J. Li, and J. Lan performed research; F.S. and J. Li contributed new reagents/analytic tools; F.S., M.I., J. Li, and J. Lan analyzed data; and F.S., J. Li, and J. Lan wrote the paper.

The authors declare no competing interest.

This article is a PNAS Direct Submission.

[1]To whom correspondence may be addressed. Email: feng-shao@hotmail.com; or jingguo.li@kemi.uu.se or jinggang.lan@epfl.ch.

[2]Present address: Ångström Laboratory, Department of Chemistry, Uppsala University, Uppsala, 75120, Sweden.

[3]Present address: Chaire de Simulation à l'Echelle Atomique (CSEA), Ecole Polytechnique Fédérale de Lausanne (EPFL), Lausanne, CH-1015, Switzerland.

This article contains supporting information online at http://www.pnas.org/lookup/suppl/doi:10.1073/pnas.2118166119/-/DCSupplemental.

Published July 14, 2022.

were observed by SEIRAS (16, 17). Regarding the formation of $C_{2(+)}$ species based on C–C couplings (C_2 pathways), FTIR provided direct evidence of the hydrogenated dimer intermediate (*OCCOH) on Cu(100) in alkaline media (20), while ATR-SEIRAS results suggested a kinetically linked dimer intermediate (*OCCO) on electrodeposited and $Cu(OH)_2$-derived Cu surfaces (21). Furthermore, X-ray–based spectroscopies offered insights into the chemical state of Cu surfaces where Cu(I) species promoted C–C coupling during pulsed CO_2RR (23). Despite recent rapid developments, simultaneous identification of these surface intermediates and understanding of adsorbate–adsorbate interactions on atomically flat Cu surfaces during $CO_{(2)}$RR continue to pose a challenge.

To gain insights into coexistent intermediates and their competitive reaction pathways, in this work we combined SHINERS with ab initio molecular dynamics (AIMD) calculations to study the CORR/COOR on Cu single-crystal electrodes in aqueous environments. As a cutting-edge spectroscopic methodology, SHINERS can conduct in situ spectroelectrochemical analysis (40 to 4,000 cm^{-1}) within a few nanometers of thickness above the electrode surfaces, where the vibrational fingerprints of surface species can be monitored with ultrahigh sensitivity (Fig. 1) (11, 25, 26). On the other hand, density functional theory (DFT)–based AIMD can take the entire electrochemical interface into account, simulating interfacial electronic structures and dynamics at every time step within a quantum-mechanical formalism, making it feasible to link computer simulations to realistic electrochemical interfaces (10, 27–32). Owing to their well-defined surface states and optical and electric field properties, Cu single-crystal surfaces are excellent models for probing electrocatalytic $CO_{(2)}$RR mechanisms at the atomic level (33). We obtained direct spectral evidence for the coexistence of intermediates of $*CO_{atop}$, $*CO_{bridge}$, *HOCCOH, *CHO, $*CO_2^-$, $*CO_3^{2-}$, *CCO, and $Cu\text{-}OH_{ad}$/$Cu\text{-}O_{ad}$ during the CORR on different Cu surfaces and in various electrolytes, and their identifications are also backed up via isotope substitution experiments and AIMD simulations. Our results provide critical mechanistic insights into the $CO_{(2)}$RR on Cu surfaces and demonstrate the competition between the C_2 pathways (*HOCCOH and *CCO species) and COOR ($*CO_2^-$ and $*CO_3^{2-}$ species) at low overpotentials (e.g., $-0.3 < U < 0.2$ V versus reversible hydrogen electrode (RHE)), as well as reveal the C_1 pathways (*CHO species) at high overpotentials (e.g., $-0.6 < U < -0.2$ V versus RHE).

Results and Discussion

Electrochemical SHINERS (EC-SHINERS) Techniques and AIMD Simulations. Fig. 1*A* illustrates the in situ EC-SHINERS approach that we employed to investigate the CORR on Cu single-crystal surfaces (*SI Appendix*, Fig. S1). Each shell-isolated nanoparticle (SHIN) was composed of a gold nanoparticle core (~55 nm) and an ultrathin SiO_2 shell (~3 nm; *SI Appendix*, Fig. S2). This core@shell strategy allowed the Au core to enhance the electromagnetic field for boosting Raman signals, while the thin SiO_2 shell was able to exclude interferences between the Au core and the surrounding chemicals (26). The integrity of its pinhole-free shell was verified in strong alkaline conditions (*SI Appendix*, Fig. S3). Prior to drop-casting these SHINs onto substrates (~20% coverage; *SI Appendix*, Fig. S2), the Cu(100), (111), and (110) single-crystal electrodes were prepared and characterized by standard procedures (*SI Appendix*, Figs. S4–S6) (34). Compared to infrared (IR) spectroscopy, which rarely records useful signals at wavenumbers below 800 cm^{-1} at the electrochemical interfaces (35), SHINERS features high sensitivities at the full-spectroscopic range (40 to 4,000 cm^{-1}; *SI Appendix*, Fig. S7). For instance, oxygen-containing species such as $Cu\text{-}O_{ad}$ (320, 393 to 400, and 630 cm^{-1}) and $Cu\text{-}OH_{ad}$ (520 to 544 cm^{-1}) can be well resolved (Fig. 2*A* and *SI Appendix*, Table S1) (15). This is also evidenced by calculations of the local electric field E (by the three dimensional–finite-difference time-domain (3D-FDTD) approach; more details in *SI Appendix*), which is greatly enhanced within the $Au@SiO_2$ particle/Cu substrate junction (Fig. 1*B*) under laser excitation (E_0) due to strong surface plasmon resonances (26). These junctions are known as hotspots, where Raman signal enhancement ($G \propto \log(|E_0/E|^4)$) is estimated to be more than six orders of magnitude, thereby facilitating the ultrasensitive in situ monitoring of trace intermediates at the electrochemical interfaces (*SI Appendix*, Note S1) (36). Without SHINs to provide sufficient enhancement, no significant Raman features can be recorded from the plain Cu(100) surface (*SI Appendix*, Fig. S8).

To elucidate intermediates observed from EC-SHINERS, we first applied static vibrational analysis based on the finite difference method to provide detailed vibrational mode assignments without considering the dynamical solvent environment (*SI Appendix*, Fig. S9 and Tables S2 and S3). For the electrochemical interfaces, however, the static vibrational analysis may not be appropriate because the dynamic interactions between the

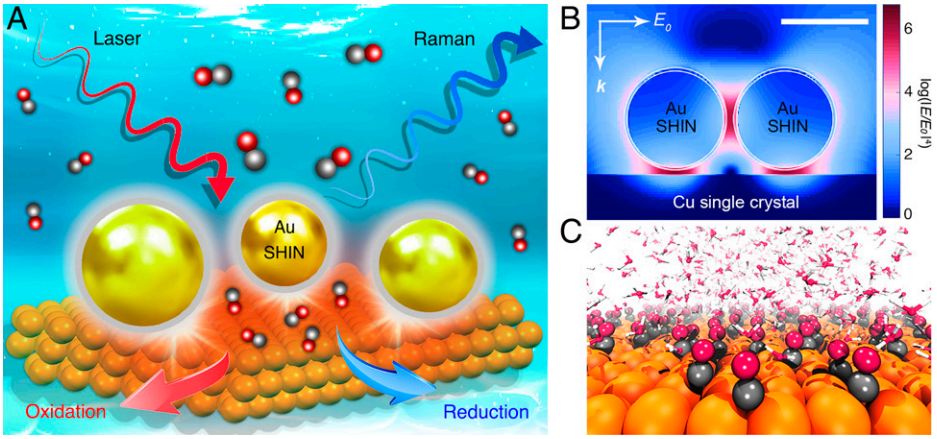

Fig. 1. In situ electrochemical SHINERS and theoretical simulation for studying the CO redox at Cu surfaces. (*A*) Schematic illustration of the in situ EC-SHINERS technique used to study the electrochemical CO redox at Cu single-crystal surfaces in various electrolytes. (*B*) 3D-FDTD simulation of the field distribution within the coupling configuration between a Cu surface and a 2 × 2 array of $Au@SiO_2$ SHINs (scale bar, 50 nm). E and E_0 denote the localized electric field and the incident electric field, respectively; the Raman enhancement factor is proportional to the fourth power of the local field enhancement ($|E/E_0|^4$); k represents the wavevector of the incident light. (*C*) Schematic representation of an AIMD simulation model, where Cu, C, O, and H atoms are presented in orange, black, red, and white colors, respectively.

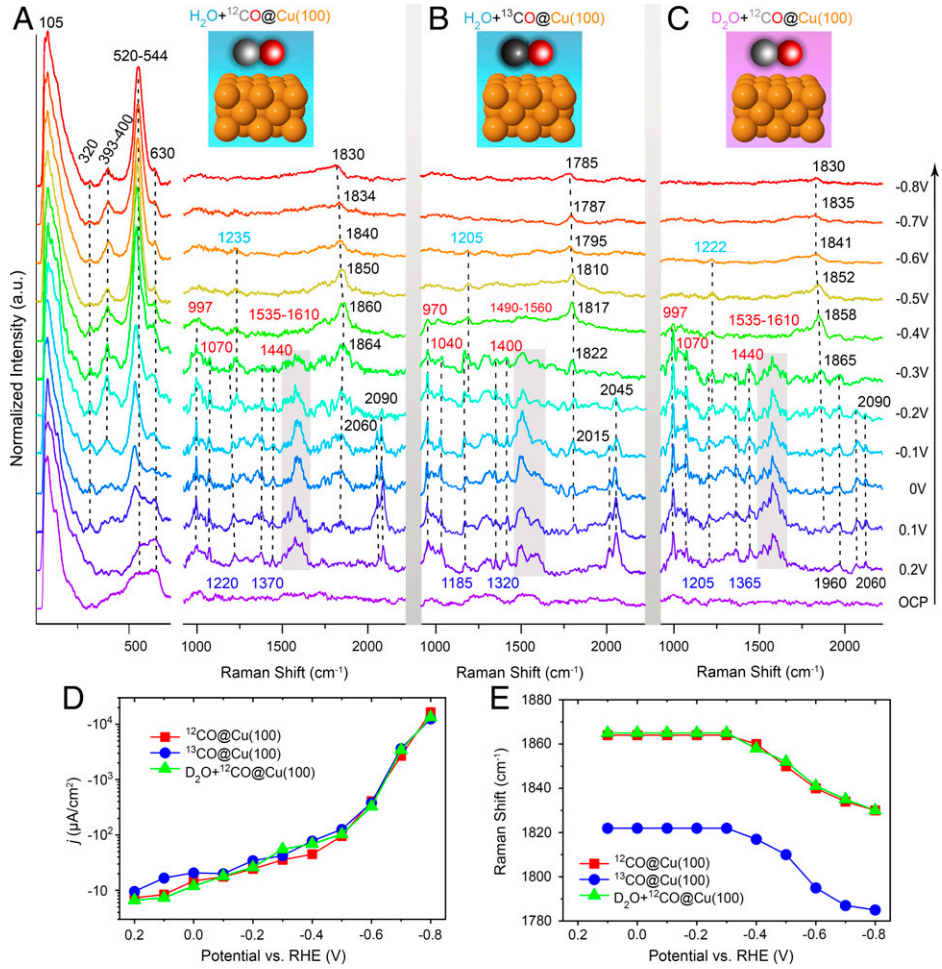

Fig. 2. In situ Raman spectra and current densities during the CO redox at Cu(100). (*A–C*) Potential-dependent EC-SHINERS spectra recorded from Cu(100) in the presence of (*A*) ^{12}CO and (*B*) ^{13}CO and (*C*) with D_2O as electrolyte in 0.1 M CsOH/OD solutions (pH = 13). These solutions are saturated with ^{12}CO or ^{13}CO gases. The Cu, ^{12}C, ^{13}C, and O atoms are presented in orange, gray, black, and red colors, respectively. All spectra are normalized to the intensity of the 105 cm^{-1} bands. a.u., arbitrary units; OCP, open circuit potential. (*D*) The total current density of Cu(100) under different conditions. (*E*) Corresponding Raman shifts for C=O stretching modes on Cu(100) under different conditions. a.u. arbitrary units.

solvent and the reaction intermediates can strongly impact the related vibration modes (31, 32). To this end, advanced AIMD simulations were further used to model atomistic structures and to predict the vibrational density of states (VDOSs) of reaction intermediates at the Cu(100)/water interface (Fig. 1*C*), which can be compared directly with operando spectroscopic measurements. Notably, the anharmonicities of vibrational modes, the intramolecular/intermolecular couplings, and the dynamics of the solvents were explicitly taken into consideration in AIMD, providing a promising tool to simulate the vibrational dynamics of surface intermediates (29, 31, 32, 37). Moreover, the AIMD can also disclose some dynamical reaction pathways in the presence of solvent molecules where static DFT calculations are not described accurately (10).

CO Adsorption. Our EC-SHINERS spectra provide rich details of reaction intermediates formed on Cu(100) during the CORR, as presented in Fig. 2. The reference spectra have not disclosed any obvious Raman features, as taken from Ar-saturated electrolyte (0.1 M CsOH, pH = 13) at open circuit potentials (~0.86 V versus RHE) and at different working potentials (*SI Appendix*, Figs. S10–S12). After the electrolyte with ^{12}CO was adequately saturated (pH = 13), distinct Raman peaks could be observed under low overpotentials (from +0.2 to −0.3 V; Fig. 2*A*). Meanwhile, low current densities were recorded (ca. > −100 μA/cm^2; Fig. 2*D*). The first conspicuous species detected by SHINERS was *CO, indicated by its C≡O stretching vibrations at 2,060 cm^{-1} (on terrace sites) and 2,090 cm^{-1} (on step sites) on Cu(100) (38–40). The later vibrational mode shifted slightly to 2,080 cm^{-1} on Cu(111) and 2,085 cm^{-1} on Cu(110), respectively, due to their different adsorbed states on the corresponding Cu facets (*SI Appendix*, Fig. S13) (41). These CO_{atop} intermediates were only detectable at potentials around 0.2 to −0.2 V (Fig. 2 and *SI Appendix*, Fig. S14) because they prefer to adsorb on the Cu surface that primarily has Cu(I) states, and they will be quickly reduced to hydrocarbons under more negative potentials (22, 42). With the ^{13}CO isotope exchange (Fig. 2*B*), the adsorbed C≡O vibrations were red-shifted to 2,015 and 2,045 cm^{-1}, as expected from the difference in $^{12}CO/^{13}CO$ isotopic masses (*SI Appendix*, Note S2) (43).

A set of bands at 1,830 to 1,864 cm^{-1}, corresponding to C=O stretching modes on bridge sites, were also continuously recorded on Cu(100) surface with a cathodic (Fig. 2*A* and *C*) and an anodic scan (*SI Appendix*, Fig. S7) (44). Their peak positions mostly remained static around 1,864 cm^{-1} at applied potentials from +0.1 to −0.3 V (Fig. 2*E*) when the current densities was low (e.g., > −50 μA/cm^2; Fig. 2*D*). The vibrational frequencies of bridge adsorption started to red-shift from around 1,864 to 1,830 cm^{-1}, with the potentials stepping from −0.3 to −0.8 V (Fig. 2*A* and *C*) and the corresponding current densities changed exponentially from ca. −50 to −1 × 10^4 μA/cm^2 (Fig. 2*D*). It

indicates that adsorbed CO is subject to the vibrational Stark effect with a Stark tuning rate of ca. 68 ± 10 cm^{-1}/V (Fig. 2*E*) due to electric field–induced changes in Cu-CO bridge bonding (45, 46). Notably, the similar Stark tuning rate was estimated to be ca. 63 ± 10 cm^{-1}/V on Cu(111) and ca. 72 ± 10 cm^{-1}/V on Cu(110) (*SI Appendix*, Fig. S13). This Stark effect can also be found from the spectra recorded on Cu(100) in the 0.1 M ^{12}CO-saturated KOH (ca. 60 ± 8 cm^{-1}/V, pH = 13.0; *SI Appendix*, Fig. S15) and LiOH (ca. 50 ± 8 cm^{-1}/V, pH = 12.3; *SI Appendix*, Fig. S15) solutions. These different Stark rates suggest that CO_{bridge} adsorption configuration is susceptible to the cation effect, which can be ascribable to the modification of the interfacial charge density and electric field due to the different cation sizes (47–50). At potentials below −0.2 V (Fig. 2*A*), there is more CO_{bridge} configuration on Cu(100). This may be explained by the ability of multiple CO coordinations to allow for an increasing population of 2π* back-donation between the adsorbed *CO and metal surfaces at more negative potentials (51). This leads to a weakening of the C-O bond and a red-shift in the vibrational frequency. However, the residual CO_{bridge}, favored on Cu(0) sites, may inhibit further hydrocarbon formation (22, 42). Moreover, these C=O vibrations red-shifted by ∼44 cm^{-1} in the ^{13}CORR at the same potentials, in line with expected $^{13}CO/^{12}CO$ vibrational frequency adjustments (Fig. 2*E* and *SI Appendix*, Note S2) (52).

Reaction Intermediates during the CORR. Two Raman peaks at 1,220 and 1,370 cm^{-1} were initially visible, and they gradually faded away with a cathodic scan from +0.2 to −0.3 V (Fig. 2*A* and *SI Appendix*, Fig. S14). Similar phenomena during the CORR was also reproduced on Cu(111), Cu(110) (*SI Appendix*, Fig. S13), or roughened polycrystalline Cu surfaces (*SI Appendix*, Figs. S16 and S17), as well as on Cu(100) in the ^{12}CO-saturated KOH (*SI Appendix*, Fig. S15), LiOH (*SI Appendix*, Fig. S15), $CsHCO_3$ (*SI Appendix*, Fig. S18), and CsCl (*SI Appendix*, Fig. S19) solutions. This is due to the fact that even Cu single-crystal facets tend to reconstruct quickly under reaction conditions (53). In particular, these two peaks were invisible in 0.1 M Ar-saturated $CsHCO_3$ solutions (pH = 9.0) at low overpotentials (from +0.2 V to −0.3 V; *SI Appendix*, Fig. S18*B*), indicating that there are no possible spectral overlaps from HCO_3^-/CO_3^{2-} species at these regions (*SI Appendix*, Note S3). The peak around 1,220 cm^{-1} was red-shifted to lower wavenumbers of around 1,185 cm^{-1} (Fig. 2*B*) and 1,205 cm^{-1} (Fig. 2*C*) in the ^{13}CO (∼35 cm^{-1}) and D_2O (∼15 cm^{-1}) isotopic experiments, respectively, which implies that the vibration mode correlated with both 'C' and 'H' atoms (*SI Appendix*, Notes S4 and S5). Meanwhile, a red-shift of ∼50 cm^{-1} (Fig. 2*B*) was observed in the ^{13}CO-labeling studies from around 1,370 cm^{-1} to 1,320 cm^{-1}, indicating that more than one 'C' atom (*SI Appendix*, Note S6) contributed to the isotope effects. According to the VDOSs predicted by AIMD simulations (Fig. 3*A*) and the experimental onset potential for the C_2 pathways (ca. −0.3 V for ethylene) under similar conditions (54), we postulate that these bands belong to vibrations of the *HOCCOH species adsorbed on Cu(100) at low overpotentials, where the bands at 1,220 cm^{-1}(1,215 cm^{-1} in the VDOSs; Fig. 3*A*) and 1,370 cm^{-1} (1,375 cm^{-1} in the VDOSs; Fig. 3*A*) can be ascribed to its -C-OH bending and -C=C- stretching modes (*SI Appendix*, Table S2), respectively. These experimental/calculated peaks are also in agreement with previous AIMD results, as reported by Cheng et al. (10). They disappeared entirely in the spectra at more negative electrode potentials (ca. < −0.4 V; Fig. 2*A*), probably due to fast consumption of the *HOCCOH intermediates during the C_2 pathways under such conditions (54).

In parallel, we also excluded assignments for both *OCCO and *OCCOH species during the C–C coupling and dimer hydrogenation. Based on our AIMD and the previous simulations (10), only *HOCCOH was predicted to be a long-lived species on Cu(100). The *OCCO species was supposed to derive from a CO–CO coupling process at neighboring sites and later react with water molecules for the formation of the *OCCOH species (Movie S1) (10). On the contrary, the uncoupled CO was almost inactive for direct hydrogenation. We estimated the radial distribution functions (RDFs) of the oxygen from CO (or C_2O_2) and hydrogen from water molecules (Fig. 3*C*). The recorded signals at 3,400 to 3,480 cm^{-1} can be attributed to the O–H stretching modes of interfacial H_2O on the Cu surface (*SI Appendix*, Fig. S7) (11). RDF features around 2.0 and 3.0 Å are for uncoupled CO molecules. Namely, the solvent water molecule is unlikely to form a hydrogen bond with surface-bonded CO. This indicates that *CO has difficulty receiving a proton directly from water molecules at low overpotentials. Indeed, recent DFT calculations have shown that CO hydrogenation to *COH/*CHO underwent a higher activation barrier than the CO dimerization pathway on Cu(211) in pH = 13 electrolytes (55, 56). The peaks of RDF for coupled C_2O_2 appeared at 1.1 Å and 1.7 Å, representing the formation of *OCCOH or *HOCCOH intermediates and a hydrogen bond between oxygen from C_2O_2 and hydrogen from the water molecule. We tracked the Mulliken charge population of the oxygen atoms from the *OCCO species (Fig. 3*D* and Movie S1). The oxygen atoms initially possessed a net charge around −0.1 |e|, and later a more negative charge around −0.3 ∼ −0.4 |e| due to electron transfer to the electrode. More negatively charged oxygen atoms contributed to a higher reactivity for receiving protons from the aqueous environment. Once the proton was received by the oxygen atom, the charge of the latter fluctuated around −0.2 ∼ −0.3 |e|. Consequently, the *OCCO and *OCCOH species (Movie S2) tended to finally form the *HOCCOH species with surface H_2O as proton sources. In other words, both intermediates were less stable than *HOCCOH. Moreover, characteristic peaks at 1,005 cm^{-1} for *OCCO (symmetric O=C–C=O stretching modes) and at 1,265 cm^{-1} for *OCCOH (-C=O stretching modes) were significantly distinguished from the bands of the *HOCCOH species at 1,220 and 1,370 cm^{-1} (Fig. 3*A* and *SI Appendix*, Table S2) (10). All the aforementioned facts further verified our assignments at 1,220 and 1,370 cm^{-1} for the *HOCCOH intermediate.

We concurrently observed a weak peak around 1,960 cm^{-1} on different Cu surfaces in 0.1 M ^{12}CO-saturated CsOH (Fig. 2*C* and *SI Appendix*, Fig. S13) and $CsHCO_3$ (1,950 cm^{-1}, *SI Appendix*, Fig. S18) solutions. It can be assigned to asymmetric C=C=O stretching modes of a surface ketene (*C=C=O) species according to the calculated VDOSs (at 1,987 cm^{-1}; *SI Appendix*, Fig. S20). Previous AIMD calculations found that the *HOCCOH at electrochemical conditions dehydrates to form a long-lived *C=C=O intermediate, especially at low overpotentials and high pH conditions (10). More recently, Luc and coworkers (57) proposed a pathway involving water incorporation into an ethenone (*CH_2CO) species to form an acetic acid (CH_3COOH) molecule, which is both thermodynamically stable and kinetically feasible based on DFT calculations. In this pathway, the *C=C=O formation starts from the *OCCOH intermediate, and it is in a dynamic equilibration with the *CH =C=O and *CH_2CO species since they show small free energy differences between each other (ca. 0.1 to 0.2 eV) (57).

It is worth noting that another set of peaks around 1,235 cm^{-1} gradually grew first, then vanished as the applied potentials became

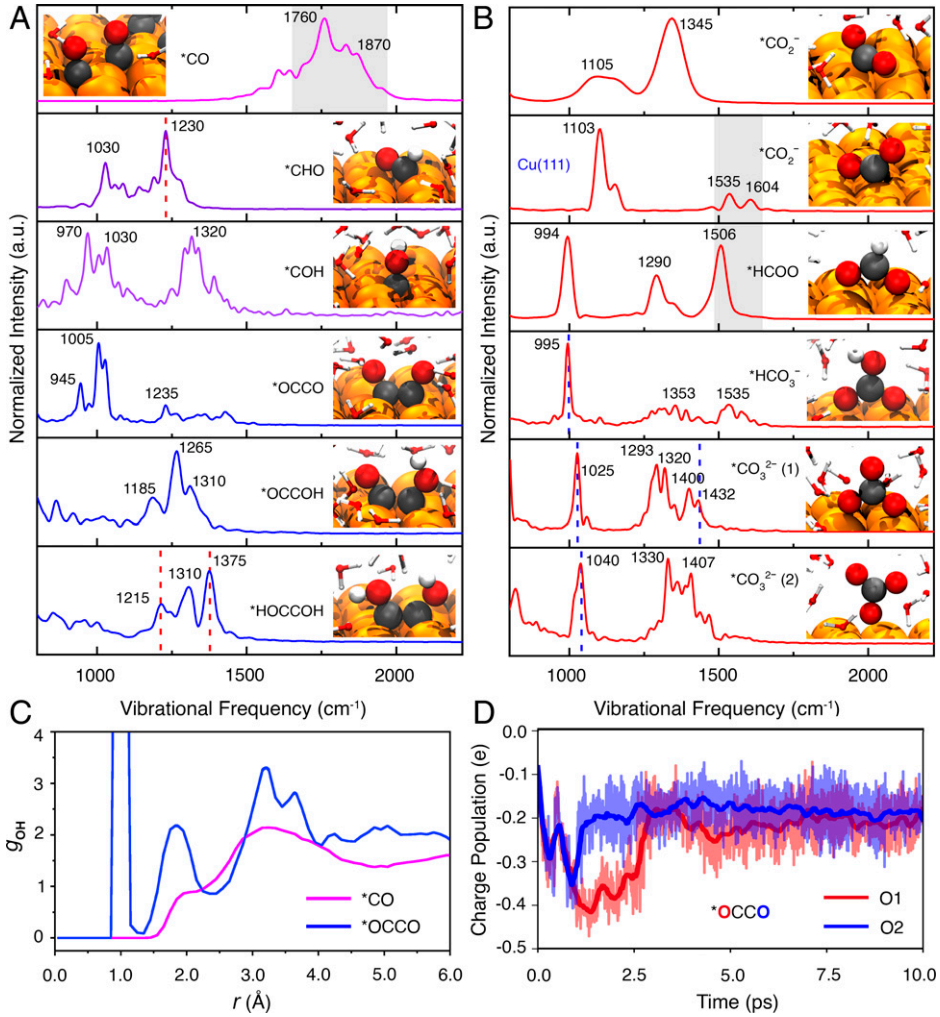

Fig. 3. Simulated properties of the reaction intermediates during the CO redox at Cu surfaces. (*A* and *B*) VDOSs as obtained from AIMD simulations and representative snapshots of typical reaction intermediates during the (*A*) CORR on Cu(100) and (*B*) COOR on Cu(100)/Cu(111). The Cu, C, O, and H atoms are presented in orange, black, red, and white colors, respectively. The dashed lines highlight good agreement between the calculated and experimental frequencies. The gray areas represent a broadband feature of these calculated VDOSs. (*C*) RDF g_{OH} of oxygen from the uncoupled CO (purple) and coupled OCCO (blue) molecules and hydrogen from the water molecules. (*D*) Mulliken charge population as a function of time for two oxygen atoms from the OCCO intermediate, where the two oxygen atoms are labeled as O1 and O2, respectively. The solid lines represent the running average of the charge populations. a.u., arbitrary units.

more negative (ca. from −0.2 to −0.6 V; Fig. 2*A* and *SI Appendix*, Fig. S14). These features were also visible in the EC-SHINERS spectra recorded on different single-crystal surfaces (*SI Appendix*, Fig. S13) and in various electrolytes (*SI Appendix*, Figs. S15, S18, and S19). In addition, this peak redshifted to 1,205 and 1,222 cm^{-1} in the ^{13}CO (~30 cm^{-1}) and D_2O (~13 cm^{-1}) labeling studies, respectively (Fig. 2*B* and *C*). This suggests that both 'C' and 'H' atoms were responsible for changing the vibrational frequencies, similar to the -C-OH stretching modes of the *HOCCOH species (Fig. 2*B* and *C*). This can be assigned to the in-plane bending mode of the *CHO species formed on Cu(100) before activation of the methane formation (with an onset potential at ca. −0.65 V) (54), as predicted by AIMD calculations (at 1,230 cm^{-1}; Fig. 3*A*). Recent DFT calculations showed that the reaction barrier of CO hydrogenation through the *CHO path was lower than that via the *COH pathway at pH = 13 on Cu(211) (55, 56), although both were kinetically inhibited in alkaline solutions (58). The CO hydrogenation to form *CHO was demonstrated to be the key step during the formation of both methane and ethylene on Cu(111) (59). Notably, a band at 1,407 cm^{-1} corresponding to *CHO was observed in the operando FTIR spectra as reported by Pérez-Gallent et al. (54), which showed disparate spectroscopic activities in various alkaline hydroxide solutions (Li, Na, K, Rb, and Cs) and on different Cu surfaces (100 and 111 facets). However, our SHINERS spectra presented corresponding Raman features at 1,235 cm^{-1} under different pH and ion conditions, owing to the distinct selection rules and cross-section for IR and Raman/SHINERS (60).

Reaction Intermediates during the COOR. Notably, significant Raman peaks appeared at 997, 1,070, 1,440, and 1,535 to 1,610 cm^{-1} regions at low potentials from +0.2 to −0.3 V (Fig. 2*A*), which are also repeatable on different single-crystal surfaces (Fig. 2*A* and *SI Appendix*, Fig. S13) and in different alkaline solutions (*SI Appendix*, Figs. S15, S18, and S19). These peaks are inconsistent with calculated VDOSs of typical long-lived CORR intermediates reported in our AIMD (e.g., *HOCCOH, *CHO, and *COH; Fig. 3*A*) or in previous simulations (e.g., *CCOH, *CHCOH, CCH, and *CCH_2) during the CORR (10). This was explained by Auer et al. (7), who suggested that Cu catalysts could electro-oxidize CO efficiently on self-activated Cu(111) surfaces in alkaline media (0.1 M NaOH). It has been proposed that both adsorbed *OH and *CO species will

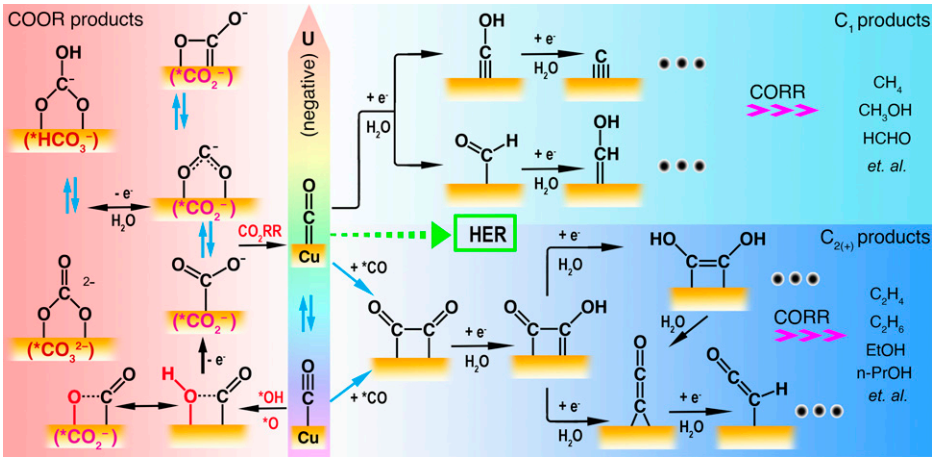

Fig. 4. Proposed reaction mechanisms for CORR versus COOR on Cu single-crystal electrodes in alkaline solutions (pH = 13). EtOH, ethanol; n-PrOH, propan-1-ol.

coexist on Cu(111) and induce the formation of undercoordinated Cu adatom clusters through surface reconstruction. These newly formed active sites are responsible for CO oxidation ($CO_{ads} + OH_{ads} \rightarrow CO_2 + H^+ + e^-$) (7). Therefore, the above-mentioned peaks originated from the intermediates introduced during the COOR in alkaline solutions at low overpotentials. This indeed was evidenced by our AIMD simulations (Fig. 3*B* and *SI Appendix*, Table S3) and previous literature (61, 62), in which peaks around 1,560 to 1,610 cm^{-1} regions were related to the asymmetry stretching of the $*CO_2^-$ species, and 997, 1,070, and 1,440 cm^{-1} peaks corresponded to surface-bound $*CO_3^{2-}$ species (*SI Appendix*, Note S7). Moreover, these peaks red-shifted correspondingly in the ^{13}CO labeling studies (Fig. 2*B*) but remained unaffected in the deuterium isotopic substitution measurement (Fig. 2*C*), indicating that they are in the deprotonation form ($*CO_3^{2-}$ and $*CO_2^-$) in strong alkaline solutions.

To further verify our assumption for COOR occurrence, more Raman signals were simultaneously recorded at low wavenumbers (e.g., a set of peaks at ca. 530 cm^{-1} on different Cu surfaces at pH = 13; Fig. 2*A* and *SI Appendix*, Figs. S21 and S22). These peaks were blue-shifted from 520 to 543 cm^{-1} with a cathodic scan from +0.2 to −0.8 V (Fig. 2*A*), implying that they were affected by the vibrational Stark effect with a Stark tuning rate of 20 ± 5 cm^{-1}/V (12). They could be assigned to O-H bending modes of the surface *OH species, which are hydrogen-bonded with surrounding water molecules, as suggested by previous Raman studies (*SI Appendix*, Table S1) (15, 63, 64). Strictly, this peak position range remained unaffected in the ^{13}CO-saturated CsOH (0.1 M) solution (*SI Appendix*, Fig. S22) but relocated to 516 to 538 cm^{-1} when D_2O was used (0.1 M ^{12}CO-saturated CsOD; *SI Appendix*, Fig. S22). When the potential holds at −0.4 V, for example, the 538 cm^{-1} peak in H_2O red-shifts (ca. 8 cm^{-1}) to 530 cm^{-1} in D_2O, hinting that these vibrational modes involve one proton (15). This is in accordance with a recent Raman observation of $CuO_x/(OH)_y$ species reported by Zhao et al. (ca. 7 cm^{-1} red-shifts) (15). However, this minor frequency shift was beyond the effect of OH/OD isotopic substitutions (*SI Appendix*, Note S8), since *OH/*OD may have a stronger hydrogen bonding with electrolyte molecules and a more robust interaction with nearby $*D_2O/*O$ species in higher alkaline solutions (pH = 13) (15). On the other hand, similar potential-dependent bands around 521 to 544 cm^{-1} were consistently recorded during the corresponding $^{13}COOR$ (*SI Appendix*, Fig. S22), excluding the involvement of 'C-containing' species.

Additional comparative experiments were conducted in the ^{12}CO- or Ar-saturated $CsHCO_3$ media (0.1 M, pH = 9.0; *SI Appendix*, Fig. S18), in which the HCO_3^- ions were the predominant species (65). Similar Raman peaks were also observed on Cu(100) at 996, 1,060, 1,440, and 1,535 to 1,670 cm^{-1} regions in both $CsHCO_3$ solutions, suggesting that these bands are more likely to be relevant to HCO_3^-/CO_3^{2-} species than to reaction intermediates (*SI Appendix*, Fig. S18). Notably, the Ar-saturated $CsHCO_3$ solution can help to eliminate dissolved CO_2 from the atmosphere (*SI Appendix*, Fig. S18). In addition, the absence of a prominent band at 1,489 cm^{-1} (symmetric CO_2 vibration mode) makes it possible to rule out the formation of Cesium salts of hydrogen oxalate (*SI Appendix*, Fig. S18) (66). Overall, we can conclude that CO can be electrochemically oxidized to CO_2-related species on Cu surfaces in alkaline solutions (CsOH) under low current densities (ca. > −100 μA/cm^2; Fig. 2*D* and *SI Appendix*, Fig. S23). The COOR proceeds through a coupling of surface-adsorbed *CO and *OH/*O species (*SI Appendix*, Tables S1 and S3) (7).

Competing Redox Reaction Pathways. During the $CO_{(2)}RR$, competing reactions on the Cu surface, for example, HER and C_1 product formation, are able to reduce the Faradaic efficiency of the desired $C_{2(+)}$ products (55, 67). These alternative reduction pathways can either reduce CO coverage or occupy exposed Cu sites, leading to limited efficiency and selectivity for C–C coupling at more negative potentials. More importantly, direct evidence of the COOR has been rarely observed in previous work, and neither has been considered in parallel with the CORR at low overpotentials. To promote the design of catalysts toward higher $C_{2(+)}$ product efficiency and selectivity, one of the key strategies is to minimize all other competitive reactions during the CORR. Based on the aforementioned intermediates identified from our in situ SHINERS spectra, we propose the competing CO redox landscape along with the applied potentials (U) in alkaline solutions (pH = 13), as shown in Fig. 4. Notably, no products may be released to any detectable level under the conditions investigated by gas chromatography (GC) or online electrochemical mass spectrometry (OLEMS) (54, 68), yet various surface intermediates on Cu(100) become recognizable via the EC-SHINERS method due to its detection sensitivity at the molecular level. As a matter of fact, C_2H_4 and CH_4 formation can even be triggered at +0.34 and +0.43 V on the RHE scale under pH = 13 conditions, respectively, as predicted by thermodynamic estimation from electrochemical half-reactions (*SI Appendix*, Tables S4 and S5) (69).

Although the abundance of product species has been below the detection limit of OLEMS and GC methods in previous systems at low overpotentials (−0.3 V < U < 0.2 V) (54, 68), we spectroscopically identified competing reactions between the CO_{atop} (2,060 and 2,090 cm^{-1}, −0.2 < U < 0.2 V) and CO_{bridge} (~1,860 cm^{-1}, −0.8 < U < 0.1 V) adsorption, as well as the COOR (997, 1,070, 1,440, and 1,535 to 1,610 cm^{-1}, −0.3 < U < 0.2 V) and the C_2 pathways (1,220, 1,370 and 1,960 cm^{-1}, −0.2 < U < 0.3 V). The COOR/C_2 intermediates gradually disappeared in SHINERS spectra because the $CO_{(2)}$RR prevailed over COOR and fewer C_2 intermediates were accumulated, with potentials becoming more negative (Fig. 2*A*). Meanwhile, although some HER intermediates (e.g., *H) were indistinguishable in the SHINERS spectra due to their small cross-section, HER was simultaneously involved in the competition to some extent (Fig. 4) (17). At potentials around −0.3 V, the C_2H_4 formation was likely detectable by OLEMS, while the typical intermediate (*CHO at 1,235 cm^{-1}, −0.6 < U < −0.3 V) for the C_1 pathways also appeared in the spectra (Fig. 2*A*) (54). When reaching the experimental onset potential of HER at ca. −0.4 V (54), HER was fully activated, and plenty of *H species interacted with the COOR/C_2-related intermediates, resulting in the vanishing of these peaks in the spectra (Fig. 2*A*). Similarly, at potentials around −0.6 V, close to the experimental onset potential of CH_4 formation (ca. −0.65 V) (54), the fast consumption of the C_1 intermediate also made its related peak (1,235 cm^{-1}) disappear in the spectra (Fig. 2*A*). Note that at potentials more negative than −0.8 V, abundant bubbles could be trapped in the gap between the working objective and the working electrode surface and thus attenuate the Raman signals (70).

Conclusions

In conclusion, by combining in situ EC-SHINERS and advanced AIMD simulations, we obtained direct spectroscopic evidence of reaction intermediates that were formed during CO redox on Cu single-crystal surfaces. Coexistent intermediates and their transformations, including $*CO_{atop}$, $*CO_{bridge}$, *HOCCOH, *CHO, $*CO_2^-$, $*CO_3^{2-}$, *CCO, and Cu-OH_{ad}/Cu-O_{ad} during COOR/CORR in alkaline electrolytes were spectroscopically identified, assignments that were further supported by a series of $^{13}CO/D_2O$ isotope substitution experiments and AIMD simulations. Potential-dependent reaction pathways (e.g., the COOR, C_2, and C_1 pathways) compete on different Cu surfaces at low overpotentials (e.g., −0.3 < U < 0.2 V versus RHE). The larger cations (e.g., Cs^+) play a more significant role in affecting the Stark tuning rate of $*CO_{bridge}$ (from −0.3 to −0.8 V) than small cations do (e.g., K^+ and Li^+) under the same conditions. The surface *OH/*O species were found to interact with the *CO and led to CO oxidation ($*CO_2^-$ and $*CO_3^{2-}$ species). AIMD results demonstrated that the VDOSs could accurately interpret representative Raman peaks of reactive intermediates at electrocatalytic interfaces, suggesting that the surface *OCCO and *OCCOH species are short-lived, and they will react fast with water, eventually forming the energetically favorable *HOCCOH intermediate. In this case, the surface H_2O molecule could serve as a strong proton donor for the *OCCO dimer protonation. This work integrated in situ spectroscopy with AIMD simulations to promote mechanistic understanding of the $CO_{(2)}$RR in the full-spectroscopic range and at the molecular scale, thus improving the design of efficient $CO_{(2)}$RR catalysts.

Materials and Methods

1. Electrochemical Raman Measurements. Chronoamperometry was performed using a Gamry reference 600 Potentiostat at room temperature. An Hg/HgO (0.1 M KOH, CHI Instruments) electrode was used as a reference electrode, and a coiled Pt wire in a homemade membrane separator (more details in *SI Appendix*, Fig. S1) was used as a counter electrode (ALS). iR (current-resistance) compensation was made using the current interrupt method. SHINs were drop-casted onto the Cu single-crystal electrodes, followed by an electrochemical cleaning with 0.1 M $NaClO_4$ (99.5%, Sigma-Aldrich) (11). A potential of −2.0 V versus Ag/AgCl was applied for the HER cleaning procedure. Each HER cleaning lasted ~1 min, and then the electrode surfaces were gently rinsed with ultrapure water. To completely clean the Cu single-crystal surfaces, this procedure was repeated three or four times (11). For a better comparison, the roughened polycrystalline Cu discs were also similarly cleaned.

In alkaline environments (0.1 M LiOH/KOH/CsOH as the electrolyte), the Hg/HgO reference electrode was used as the reference electrode. All potentials were converted to versus RHE, referring to the Nernst equation (71):

$$E_{RHE} = E_{Hg/HgO} + 0.059 * pH + E^0{}_{Hg/HgO}$$

where $E_{Hg/HgO}$ is the measured potential and $E^0{}_{Hg/HgO} = 0.096$ V, which was calibrated by a standard RHE electrode (Hydroflex ET070, eDAQ) in the 0.1 M KOH solution after 2-h N_2 bubbling at pH = 13 and under room temperature:

$$E_{RHE} \approx E_{SHE} + 0.86 \text{ V}$$

Otherwise, the Ag/AgCl reference electrode was used as the reference electrode. All related potentials were then converted to be versus RHE, referring to the Nernst equation (71):

$$E_{RHE} = E_{Ag/AgCl} + 0.059 * pH + E^0{}_{Ag/AgCl}$$

where $E_{Ag/AgCl}$ is the measured potential and $E^0{}_{Ag/AgCl} = 0.1976$ V at 25 °C.

SHINERS spectra were recorded using a Raman microscopy system (Modular system, Horiba Jobin Yvon) at room temperature. The electrochemical cell configuration was reported in our previous work (*SI Appendix*, Fig. S1) (72). A 632.8-nm He–Ne laser (CVI Melles Griot) was used as the excitation source. An epi-illumination microscope (Olympus Model U-5RE-2) with a water immersion objective (Olympus LUMFL, 60×, numerical aperture = 1.10) was used to focus and collect the incident and scattered laser light during electrochemical measurements. An optically transparent Teflon film (13-μm thickness, American Durafilm) was used to cover and protect the objective from the corrosive electrolytes. The backscattered light was filtered through an edge filter and directed into a spectrograph (iHR320)/charge-coupled device detector (Synapse CCD). Before in situ Raman spectroscopy measurements, all electrolytes were purged by CO gas over 3 h. The CO flow rate was set to 10 sccm using a Brooks GF40 mass flow controller. All SHINERS spectra were acquired from at least three different spots with three repeats each. Each presented spectrum is an average of acquired spectra with a collection time of 20 s each. The low-frequency band at 105 cm^{-1} is characteristic of the optical fibers used in our spectrometer and was used as a normalization reference and internal standard to compensate for differences in signal intensities due to laser alignment (more details in *SI Appendix*, Section 3.4).

2. DFT and AIMD Computational Details. All calculations were carried out using CP2K code (73). The electronic structure was described using Perdew–Burke-Ernzerhof (PBE) functional (74) with D3 correction (75) within the Gaussian and plane waves framework. Molecular orbitals of the valence electrons were expanded into DZVP-MOLOPT-SR-GTH basis sets (76), while atomic core electrons were described through Goedecker-Teter-Hutter pseudopotentials (77). The plane-wave basis set was truncated at the energy cutoff of 500 Ry. For static calculations, tight geometry optimization was employed by DFT methods. The vibrational analysis was performed using the finite difference method. The structures were optimized using a tight self consistent field threshold of 1E-7 arbitrary units. The increment to construct the Hessian was set to 1E-3 Bohr.

All AIMD simulations were performed using the canonical ensemble at 300 K. To achieve efficient canonical sampling while maintaining the dynamics, we applied a stochastic velocity-rescaling thermostat (78) with a time step of 0.5 fs and a constant temperature sampling enforced with a time constant of 100 fs. The simulation cell system consisted of a four-layer (6 × 6) (100) surface slab where the adsorbates were in contact with 134 explicit water molecules, which was sufficient to reproduce the proper solvation environment. A vacuum region of about 30 Å was introduced to decouple the periodic images in the Z direction. The dipole correction scheme was applied along the Z direction (79). The simulations

were carried out by keeping the bottom two metal layers fixed to maintain the bulk behavior of the inner part of the slab.

We first prepared the surface intermediates by optimizing their geometries adsorbed on Cu(100). The structures were first optimized using static DFT calculations. The vibrational analysis was based on the optimized geometry and summarized in *SI Appendix*, Tables S2 and S3. Starting from the optimized geometry, we further included explicit solvent molecules in the system and ran AIMD simulations. The water film was added and equilibrated for about 5 ps, keeping the intermediates and Cu surface fixed. The production runs were about 10 ps for each intermediate. The prediction of vibrational spectra by MD methods was obtained by a Fourier transform of the autocorrelation function. Due to the high cost, only individual surface species were taken into account during the AIMD simulations (*SI Appendix*, Note S9 and Fig. S24). Moreover, further AIMD calculations of typical intermediates (e.g., *HOCCOH and $*HCO_3^-$) indicated that their vibrational frequencies were pretty close to each other, whether or not the cation effect (Cs^+) and potential bias (U) were considered in the models (*SI Appendix*, Note S10 and Fig. S25). The power spectrum, also known as the VDOSs, featured all vibrational frequencies of the system and applied no selection rules (more details in *SI Appendix*, Section S3.5) (80):

$$\mathrm{VDOSs}(\omega) = \int \mathrm{v}(\tau)\mathrm{v}(\mathrm{t}+\tau)_\tau \mathrm{e}^{-\mathrm{i}\omega\mathrm{t}}\mathrm{dt}$$

where the $\mathrm{v}(\tau)$ is the velocity of the nuclei at starting time τ and $\mathrm{v}(\mathrm{t}+\tau)_\tau$ is the velocity of nuclei at time $\mathrm{t}+\tau$.

Data Availability. All study data are included in the article and/or supporting information. The simulation data generated and analyzed for this work are available at https://archive.materialscloud.org (DOI: 10.24435/materialscloud:sy-wx) (81).

ACKNOWLEDGMENTS. We acknowledge the Ministry of Education, Singapore (Grant No. R143-000-B52-114) and the Marie-Skłodowska-Curie Individual Fellowship (Grant No. 841653-2DvdWHs) for financial support of this work. We thank the Swiss National Science Foundation for funding and the University Research Priority Program for solar light to chemical energy conversion of the University of Zurich. This work was also supported by a grant from the Swiss National Supercomputing Centre under Project ID uzh1, s965, and s1110. The authors especially thank Prof. Dr. Boon Siang Yeo (National University of Singapore) and Prof. Dr. Jürg Hutter (University of Zurich) for their great help and support.

Author affiliations: [a]State Key Laboratory of Materials-Oriented Chemical Engineering, College of Chemical Engineering, Nanjing Tech University, Nanjing, 211816, China; [b]Department of Physics and Astronomy, National Graphene Institute, University of Manchester, Manchester, M13 9PL, UK; [c]Department of Chemistry, Faculty of Science, National University of Singapore, Singapore 117543, Singapore; [d]Solar Energy Research Institute of Singapore, National University of Singapore, Singapore 117574, Singapore; and [e]Department of Chemistry, University of Zurich, Zurich 8057, Switzerland

1. Y. Y. Birdja *et al.*, Advances and challenges in understanding the electrocatalytic conversion of carbon dioxide to fuels. *Nat. Energy* **4**, 732–745 (2019).
2. A. D. Handoko, F. Wei, Jenndy, B. S. Yeo, Z. W. Seh, Understanding heterogeneous electrocatalytic carbon dioxide reduction through operando techniques. *Nat. Catal.* **1**, 922–934 (2018).
3. S. Nitopi *et al.*, Progress and perspectives of electrochemical CO_2 reduction on copper in aqueous electrolyte. *Chem. Rev.* **119**, 7610–7672 (2019).
4. A. J. Göttle, M. T. M. Koper, Proton-coupled electron transfer in the electrocatalysis of CO_2 reduction: Prediction of sequential *vs.* concerted pathways using DFT. *Chem. Sci.* **8**, 458–465 (2017).
5. F. Calle-Vallejo, M. T. M. Koper, Theoretical considerations on the electroreduction of CO to C_2 species on Cu(100) electrodes. *Angew. Chem. Int. Ed. Engl.* **52**, 7282–7285 (2013).
6. P. Farinazzo Bergamo Dias Martins *et al.*, Hydrogen evolution reaction on copper: Promoting water dissociation by tuning the surface oxophilicity. *Electrochem. Commun.* **100**, 30–33 (2019).
7. A. Auer *et al.*, Self-activation of copper electrodes during CO electro-oxidation in alkaline electrolyte. *Nat. Catal.* **3**, 797–803 (2020).
8. A. A. Gokhale, J. A. Dumesic, M. Mavrikakis, On the mechanism of low-temperature water gas shift reaction on copper. *J. Am. Chem. Soc.* **130**, 1402–1414 (2008).
9. Y.-X. Wang, G.-C. Wang, A systematic theoretical study of water gas shift reaction on Cu(111) and Cu(110): Potassium effect. *ACS Catal.* **9**, 2261–2274 (2019).
10. T. Cheng, H. Xiao, W. A. Goddard III, Full atomistic reaction mechanism with kinetics for CO reduction on Cu(100) from ab initio molecular dynamics free-energy calculations at 298 K. *Proc. Natl. Acad. Sci. U.S.A.* **114**, 1795–1800 (2017).
11. C.-Y. Li *et al.*, In situ probing electrified interfacial water structures at atomically flat surfaces. *Nat. Mater.* **18**, 697–701 (2019).
12. I. V. Chernyshova, P. Somasundaran, S. Ponnurangam, On the origin of the elusive first intermediate of CO_2 electroreduction. *Proc. Natl. Acad. Sci. U.S.A.* **115**, E9261–E9270 (2018).
13. S. Jiang, K. Klingan, C. Pasquini, H. Dau, New aspects of operando Raman spectroscopy applied to electrochemical CO_2 reduction on Cu foams. *J. Chem. Phys.* **150**, 041718 (2019).
14. M. He *et al.*, Oxygen induced promotion of electrochemical reduction of CO_2 via co-electrolysis. *Nat. Commun.* **11**, 3844 (2020).
15. Y. Zhao *et al.*, Speciation of Cu surfaces during the electrochemical CO reduction reaction. *J. Am. Chem. Soc.* **142**, 9735–9743 (2020).
16. A. Wuttig *et al.*, Tracking a common surface-bound intermediate during CO_2-to-fuels catalysis. *ACS Cent. Sci.* **2**, 522–528 (2016).
17. J. Heyes, M. Dunwell, B. Xu, CO_2 reduction on cu at low overpotentials with surface-enhanced in situ spectroscopy. *J. Phys. Chem. C* **120**, 17334–17341 (2016).
18. K. Yang, R. Kas, W. A. Smith, In situ infrared spectroscopy reveals persistent alkalinity near electrode surfaces during CO_2 electroreduction. *J. Am. Chem. Soc.* **141**, 15891–15900 (2019).
19. S. Zhu, T. Li, W.-B. Cai, M. Shao, CO_2 electrochemical reduction as probed through infrared spectroscopy. *ACS Energy Lett.* **4**, 682–689 (2019).
20. E. Pérez-Gallent, M. C. Figueiredo, F. Calle-Vallejo, M. T. M. Koper, Spectroscopic observation of a hydrogenated CO dimer intermediate during CO reduction on Cu(100) electrodes. *Angew. Chem. Int. Ed. Engl.* **56**, 3621–3624 (2017).
21. Y. Kim *et al.*, Time-resolved observation of C–C coupling intermediates on Cu electrodes for selective electrochemical CO_2 reduction. *Energy Environ. Sci.* **13**, 4301–4311 (2020).
22. T.-C. Chou *et al.*, Controlling the oxidation state of the Cu electrode and reaction intermediates for electrochemical CO_2 reduction to ethylene. *J. Am. Chem. Soc.* **142**, 2857–2867 (2020).
23. R. M. Arán-Ais, F. Scholten, S. Kunze, R. Rizo, B. Roldan Cuenya, The role of in situ generated morphological motifs and Cu(i) species in C^{2+} product selectivity during CO_2 pulsed electroreduction. *Nat. Energy* **5**, 317–325 (2020).
24. N. Heidary, K. H. Ly, N. Kornienko, Probing CO_2 conversion chemistry on nanostructured surfaces with operando vibrational spectroscopy. *Nano Lett.* **19**, 4817–4826 (2019).
25. J.-C. Dong *et al.*, In situ Raman spectroscopic evidence for oxygen reduction reaction intermediates at platinum single-crystal surfaces. *Nat. Energy* **4**, 60–67 (2019).
26. J.-F. Li, Y.-J. Zhang, S.-Y. Ding, R. Panneerselvam, Z.-Q. Tian, Core-shell nanoparticle-enhanced Raman spectroscopy. *Chem. Rev.* **117**, 5002–5069 (2017).
27. D. Marx, Proton transfer 200 years after von Grotthuss: Insights from ab initio simulations. *ChemPhysChem* **7**, 1848–1870 (2006).
28. A. Bagger, L. Arnarson, M. H. Hansen, E. Spohr, J. Rossmeisl, Electrochemical CO reduction: A property of the electrochemical interface. *J. Am. Chem. Soc.* **141**, 1506–1514 (2019).
29. J. Lan, J. Hutter, M. Iannuzzi, First-principles simulations of an aqueous CO/Pt(111) interface. *J. Phys. Chem. C* **122**, 24068–24076 (2018).
30. J. Lan, V. V. Rybkin, M. Iannuzzi, Ionization of water as an effect of quantum delocalization at aqueous electrode interfaces. *J. Phys. Chem. Lett.* **11**, 3724–3730 (2020).
31. T. Cheng, A. Fortunelli, W. A. Goddard III, Reaction intermediates during operando electrocatalysis identified from full solvent quantum mechanics molecular dynamics. *Proc. Natl. Acad. Sci. U.S.A.* **116**, 7718–7722 (2019).
32. S. Naserifar, Y. Chen, S. Kwon, H. Xiao, W. A. Goddard, Artificial intelligence and QM/MM with a polarizable reactive force field for next-generation electrocatalysts. *Matter* **4**, 195–216 (2021).
33. A. Kolodziej, P. Rodriguez, A. Cuesta, "Single-crystal surfaces as model electrocatalysts for CO_2 reduction" in *Electrochemical Reduction of Carbon Dioxide: Overcoming the Limitations of Photosynthesis* (The Royal Society of Chemistry, 2018), pp. 88–110.
34. Y. Huang, A. D. Handoko, P. Hirunsit, B. S. Yeo, Electrochemical reduction of CO_2 using copper single-crystal surfaces: Effects of CO* coverage on the selective formation of ethylene. *ACS Catal.* **7**, 1749–1756 (2017).
35. C.-Y. Li *et al.*, In situ monitoring of electrooxidation processes at gold single crystal surfaces using shell-isolated nanoparticle-enhanced Raman spectroscopy. *J. Am. Chem. Soc.* **137**, 7648–7651 (2015).
36. E. C. Le Ru, E. Blackie, M. Meyer, P. G. Etchegoin, Surface enhanced Raman scattering enhancement factors: A comprehensive study. *J. Phys. Chem. C* **111**, 13794–13803 (2007).
37. Y. Nagata, S. Yoshimune, C.-S. Hsieh, J. Hunger, M. Bonn, Ultrafast vibrational dynamics of water disentangled by reverse nonequilibrium ab initio molecular dynamics simulations. *Phys. Rev. X* **5**, 021002 (2015).
38. C. M. Gunathunge *et al.*, Spectroscopic observation of reversible surface reconstruction of copper electrodes under CO_2 reduction. *J. Phys. Chem. C* **121**, 12337–12344 (2017).
39. A. S. Malkani, M. Dunwell, B. Xu, Operando spectroscopic investigations of copper and oxide-derived copper catalysts for electrochemical CO reduction. *ACS Catal.* **9**, 474–478 (2019).
40. P. Hollins, The influence of surface defects on the infrared spectra of adsorbed species. *Surf. Sci. Rep.* **16**, 51–94 (1992).
41. K. M. Gameel, I. M. Sharafeldin, A. U. Abourayya, A. H. Biby, N. K. Allam, Unveiling CO adsorption on Cu surfaces: New insights from molecular orbital principles. *Phys. Chem. Chem. Phys.* **20**, 25892–25900 (2018).
42. C. M. Gunathunge, V. J. Ovalle, Y. Li, M. J. Janik, M. M. Waegele, Existence of an electrochemically inert CO population on Cu electrodes in alkaline pH. *ACS Catal.* **8**, 7507–7516 (2018).
43. M. F. Mrozek, H. Luo, M. J. Weaver, Formic acid electrooxidation on platinum-group metals: Is adsorbed carbon monoxide solely a catalytic poison? *Langmuir* **16**, 8463–8469 (2000).
44. X. Chang, Y. Zhao, B. Xu, pH dependence of Cu surface speciation in the electrochemical CO reduction reaction. *ACS Catal.* **10**, 13737–13747 (2020).
45. M. Head-Gordon, J. C. Tully, Electric field effects on chemisorption and vibrational relaxation of CO on Cu(100). *Chem. Phys.* **175**, 37–51 (1993).
46. P. Zhang, Y. Wei, J. Cai, Y.-X. Chen, Z.-Q. Tian, Nonlinear Stark effect observed for carbon monoxide chemisorbed on gold core/palladium shell nanoparticle film electrodes, using in situ surface-enhanced Raman spectroscopy. *Chin. J. Catal.* **37**, 1156–1165 (2016).
47. S. Ringe *et al.*, Understanding cation effects in electrochemical CO_2 reduction. *Energy Environ. Sci.* **12**, 3001–3014 (2019).
48. J. Resasco *et al.*, Promoter effects of alkali metal cations on the electrochemical reduction of carbon dioxide. *J. Am. Chem. Soc.* **139**, 11277–11287 (2017).
49. M. R. Singh, Y. Kwon, Y. Lum, J. W. Ager III, A. T. Bell, Hydrolysis of electrolyte cations enhances the electrochemical reduction of CO_2 over Ag and Cu. *J. Am. Chem. Soc.* **138**, 13006–13012 (2016).
50. J. Li, X. Li, C. M. Gunathunge, M. M. Waegele, Hydrogen bonding steers the product selectivity of electrocatalytic CO reduction. *Proc. Natl. Acad. Sci. U.S.A.* **116**, 9220–9229 (2019).

51. S. L. Yau, X. Gao, S. C. Chang, B. C. Schardt, M. J. Weaver, Atomic-resolution scanning tunneling microscopy and infrared spectroscopy as combined in situ probes of electrochemical adlayer structure: Carbon monoxide on rhodium (111). *J. Am. Chem. Soc.* **113**, 6049–6056 (1991).
52. M. W. Severson, C. Stuhlmann, I. Villegas, M. J. Weaver, Dipole–dipole coupling effects upon infrared spectroscopy of compressed electrochemical adlayers: Application to the Pt(111)/CO system. *J. Chem. Phys.* **103**, 9832–9843 (1995).
53. F. Scholten, K. C. Nguyen, J. P. Bruce, M. Heyde, B. Roldan Cuenya, Identifying structure-selectivity correlations in the electrochemical reduction of CO_2: A comparison of well-ordered atomically clean and chemically etched copper single-crystal surfaces. *Angew. Chem. Int. Ed. Engl.* **60**, 19169–19175 (2021).
54. E. Pérez-Gallent, G. Marcandalli, M. C. Figueiredo, F. Calle-Vallejo, M. T. M. Koper, Structure- and potential-dependent cation effects on CO reduction at copper single-crystal electrodes. *J. Am. Chem. Soc.* **139**, 16412–16419 (2017).
55. X. Liu *et al.*, pH effects on the electrochemical reduction of $CO_{(2)}$ towards C_2 products on stepped copper. *Nat. Commun.* **10**, 32 (2019).
56. X. Liu *et al.*, Understanding trends in electrochemical carbon dioxide reduction rates. *Nat. Commun.* **8**, 15438 (2017).
57. W. Luc *et al.*, Two-dimensional copper nanosheets for electrochemical reduction of carbon monoxide to acetate. *Nat. Catal.* **2**, 423–430 (2019).
58. H. Xiao, T. Cheng, W. A. Goddard III, R. Sundararaman, Mechanistic explanation of the pH dependence and onset potentials for hydrocarbon products from electrochemical reduction of CO on Cu (111). *J. Am. Chem. Soc.* **138**, 483–486 (2016).
59. K. J. P. Schouten, Z. Qin, E. Pérez Gallent, M. T. M. Koper, Two pathways for the formation of ethylene in CO reduction on single-crystal copper electrodes. *J. Am. Chem. Soc.* **134**, 9864–9867 (2012).
60. R. Aroca, *Surface-Enhanced Vibrational Spectroscopy* (Wiley, 2006).
61. L. Wang, K. Gupta, J. B. M. Goodall, J. A. Darr, K. B. Holt, In situ spectroscopic monitoring of CO_2 reduction at copper oxide electrode. *Faraday Discuss.* **197**, 517–532 (2017).
62. H. Li, P. Wei, D. Gao, G. Wang, In situ Raman spectroscopy studies for electrochemical CO_2 reduction over Cu catalysts. *Curr. Opin. Green Sustain. Chem.* **34**, 100589 (2022).
63. N. Bodappa *et al.*, Early stages of electrochemical oxidation of Cu(111) and polycrystalline Cu surfaces revealed by *in situ* Raman spectroscopy. *J. Am. Chem. Soc.* **141**, 12192–12196 (2019).
64. G. Niaura, Surface-enhanced Raman spectroscopic observation of two kinds of adsorbed OH^- ions at copper electrode. *Electrochim. Acta* **45**, 3507–3519 (2000).
65. C. B. Andersen, Understanding carbonate equilibria by measuring alkalinity in experimental and natural systems. *J. Geosci. Educ.* **50**, 389–403 (2002).
66. R. E. Dinnebier, S. Vensky, M. Panthöfer, M. Jansen, Crystal and molecular structures of alkali oxalates: First proof of a staggered oxalate anion in the solid state. *Inorg. Chem.* **42**, 1499–1507 (2003).
67. T. Kim, G. T. R. Palmore, A scalable method for preparing Cu electrocatalysts that convert CO_2 into C_{2+} products. *Nat. Commun.* **11**, 3622 (2020).
68. L. Wang *et al.*, Electrochemical carbon monoxide reduction on polycrystalline copper: Effects of potential, pressure, and pH on selectivity toward multicarbon and oxygenated products. *ACS Catal.* **8**, 7445–7454 (2018).
69. K. P. Kuhl *et al.*, Electrocatalytic conversion of carbon dioxide to methane and methanol on transition metal surfaces. *J. Am. Chem. Soc.* **136**, 14107–14113 (2014).
70. Y. Deng, B. S. Yeo, Characterization of electrocatalytic water splitting and CO_2 reduction reactions using in situ/operando Raman spectroscopy. *ACS Catal.* **7**, 7873–7889 (2017).
71. J. Zhu *et al.*, Ferric citrate-derived N-doped hierarchical porous carbons for oxygen reduction reaction and electrochemical supercapacitors. *Carbon* **115**, 1–10 (2017).
72. D. Ren *et al.*, Selective electrochemical reduction of carbon dioxide to ethylene and ethanol on copper(I) oxide catalysts. *ACS Catal.* **5**, 2814–2821 (2015).
73. T. D. Kühne *et al.*, CP2K: An electronic structure and molecular dynamics software package–Quickstep: Efficient and accurate electronic structure calculations. *J. Chem. Phys.* **152**, 194103 (2020).
74. J. P. Perdew, K. Burke, M. Ernzerhof, Generalized gradient approximation made simple. *Phys. Rev. Lett.* **77**, 3865–3868 (1996).
75. S. Grimme, Semiempirical GGA-type density functional constructed with a long-range dispersion correction. *J. Comput. Chem.* **27**, 1787–1799 (2006).
76. J. VandeVondele, J. Hutter, Gaussian basis sets for accurate calculations on molecular systems in gas and condensed phases. *J. Chem. Phys.* **127**, 114105 (2007).
77. S. Goedecker, M. Teter, J. Hutter, Separable dual-space Gaussian pseudopotentials. *Phys. Rev. B Condens. Matter* **54**, 1703–1710 (1996).
78. G. Bussi, D. Donadio, M. Parrinello, Canonical sampling through velocity rescaling. *J. Chem. Phys.* **126**, 014101 (2007).
79. L. Bengtsson, Dipole correction for surface supercell calculations. *Phys. Rev. B* **59**, 12301–12304 (1999).
80. M. Thomas, M. Brehm, R. Fligg, P. Vöhringer, B. Kirchner, Computing vibrational spectra from ab initio molecular dynamics. *Phys. Chem. Chem. Phys.* **15**, 6608–6622 (2013).
81. F. Shao *et al.*, In situ spectroelectrochemical probing of CO redox landscape on copper single-crystal surfaces. Materials Cloud. https://archive.materialscloud.org. Accessed 28 June 2022.